The mean velocity profile of a smooth-flat-plate turbulent boundary layer at high Reynolds number

GHANEM F. OWEIS[2]†, ERIC S. WINKEL[1]‡,
JAMES M. CUTBRITH[3]¶, STEVEN L. CECCIO[1],
MARC PERLIN[4] AND DAVID R. DOWLING[1]‖

[1]Department of Mechanical Engineering, University of Michigan, Ann Arbor, MI 48109, USA

[2]Department of Mechanical Engineering, Faculty of Engineering and Architecture, American University of Beirut, PO Box 11-0236, Riad El Solh, Beirut 1107 2020, Lebanon

[3]Carderock Division, Naval Surface Warfare Center, W. B. Morgan Large Cavitation Channel, 3001 Harbor Avenue, Memphis, TN 38113, USA

[4]Department of Naval Architecture and Marine Engineering, University of Michigan, Ann Arbor, MI 48109, USA

Smooth flat-plate turbulent boundary layers (TBLs) have been studied for nearly a century. However, there is a relative dearth of measurements at Reynolds numbers typical of full-scale marine and aerospace transportation systems ($Re_\theta = U_e\theta/\nu > 10^5$, where U_e = free-stream speed, θ = TBL momentum thickness and ν = kinematic viscosity). This paper presents new experimental results for the TBL that forms on a smooth flat plate at nominal Re_θ values of 0.5×10^5, 1.0×10^5 and 1.5×10^5. Nominal boundary layer thicknesses (δ) were 80–90 mm, and Karman numbers (δ^+) were 17 000, 32 000 and 47 000, respectively. The experiments were conducted in the William B. Morgan Large Cavitation Channel on a polished ($k^+ < 0.2$) flat-plate test model 12.9 m long and 3.05 m wide at water flow speeds up to 20 m s^{-1}. Direct measurements of static pressure and mean wall shear stress were obtained with pressure taps and floating-plate skin friction force balances. The TBL developed a mild favourable pressure gradient that led to a streamwise flow speed increase of ∼2.5 % over the 11 m long test surface, and was consistent with test section sidewall and model surface boundary-layer growth. At each Re_θ, mean streamwise velocity profile pairs, separated by 24 cm, were measured more than 10 m from the model's leading edge using conventional laser Doppler velocimetry. Between these profile pairs, a unique near-wall implementation of particle tracking velocimetry was used to measure the near-wall velocity profile. The composite profile measurements span the wall-normal coordinate range from $y^+ < 1$ to $y > 2\delta$. To within experimental uncertainty, the measured mean velocity profiles can be fit using traditional zero-pressure-gradient (ZPG) TBL asymptotics with some modifications for the mild favourable pressure gradient. The fitted profile pairs satisfy the von-Kármán momentum integral equation to within 1 %. However, the profiles reported here show distinct differences from equivalent ZPG profiles. The

† Formerly at the University of Michigan, Ann Arbor, MI 48109, USA
‡ Present address: Design Research Engineering, Novi, MI 48377, USA
¶ Present address: Mainstream Engineering Corporation, Rockledge, FL 32955, USA
‖ Email address for correspondence: drd@umich.edu

near-wall indicator function has more prominent extrema, the log-law constants differ slightly, and the profiles' wake component is less pronounced.

Key words: turbulent boundary layers

1. Introduction

Turbulent boundary layers (TBLs) are ubiquitous in both natural and human-engineered fluid flows. They commonly set heat and mass transfer rates in the ocean and atmosphere, and are often a critical factor in determining the efficiency and performance of transportation systems. The simplest possible boundary layer occurs as uniform unidirectional flow moves over a smooth flat surface parallel to the flow direction. This boundary layer will be turbulent if the Reynolds number of the flow is sufficiently large to sustain turbulence, and an intentional or naturally occurring disturbance has caused transition from laminar to turbulent flow.

Given the importance of the phenomena and the simplicity of the flow geometry, flat-plate TBLs have been investigated for the greater part of the last century. Much is known about the mean and fluctuating components of flat-plate TBL flow from controlled laboratory-scale investigations conducted at momentum-thickness-based Reynolds numbers $Re_\theta = U_e\theta/\nu < 10^4$, where U_e is the local exterior or free-stream flow speed, θ is the momentum thickness of the boundary layer and ν is the kinematic viscosity of the fluid. Additional investigations conducted in atmospheric boundary layers and in special testing facilities at higher Reynolds numbers – where the investigations cannot be as well-controlled or as complete as the laboratory-scale studies – have allowed scaling laws developed from the laboratory studies, the governing equations and dimensional reasoning to be at least partially evaluated at the much higher Reynolds numbers, $Re_\theta > 10^6$, reached by full-scale marine and aerospace transportation systems, and by atmospheric and oceanic flows. The primary purpose of this paper is to report measured mean streamwise velocity profiles for the TBL that develops on a smooth flat plate under well-controlled conditions at $Re_\theta \cong 0.55 \times 10^5$, 1.05×10^5, and 1.53×10^5, (or, alternatively, in terms of the downstream-distance-based Reynolds number, $Re_x \cong 0.73 \times 10^8$, 1.45×10^8 and 2.2×10^8). The reported profile measurements span the wall-normal-coordinate (y) range from $y/l_v = y^+ < 1$ to $y/\delta > 2$, where $l_v = \nu\sqrt{\rho/\tau_w}$ is the usual viscous wall unit, ρ is the fluid density, τ_w is the wall shear stress, and δ is the overall boundary-layer thickness. At the highest Re, the outer-to-inner length-scale ratio, $\delta/l_v = \delta^+$, is $\sim 50\,000$.

Although the flat-plate geometry is idealized compared to that of practical aerodynamic and hydrodynamic devices, the structure and scaling of flat-plate TBLs remain important because moderate-Reynolds-number results are commonly scaled when designing or predicting the performance of fluid dynamic devices that operate at high-Reynolds numbers where experimental measurements are sparse or non-existent. Furthermore, the numerical values and functional forms used in computational models of wall-bounded turbulence are based on the flow structure and empirical constants (κ and B) determined from TBL studies (see Launder & Spalding 1972 or Pope 2000). Thus, the validity of such models is enhanced when the empirical constants are known to be valid over as large a Reynolds-number range as possible.

The published literature on the topic of TBLs is extensive and the functional form(s) and scaling for TBL mean velocity profiles remain an area of active research.

Review articles (Sreenivasan 1989; Gad-el-Hak & Bandyopadhyay 1994; Fernholz & Findley 1996; McKeon 2007; Marusic *et al.* 2010) and recent texts (Pope 2000; White 2006) provide a starting point for sorting and assimilating this material. During the last two decades or so, a variety of new interpretations and potential revisions to the classical understanding of TBL scaling and flow structure have been derived and/or proposed. These include (i) new scaling laws for the mean profile and turbulence quantities (George & Castillo 1997; Marusic, Uddin & Perry 1997; DeGraaff & Eaton 2000; Marusic & Kunkel 2003; Lindgren, Österlund & Johansson 2004), (ii) revisions to the classical layer structure of TBLs (Fife *et al.* 2005; Wei *et al.* 2005) and (iii) log-law and power-law fitting analysis (Barenblatt, Chorin & Prostokishin 2000; Österlund, Johansson & Nagib 2000*a*; Österlund *et al.* 2000*b*; Afzal 2001; Panton 2002; Buschmann & Gad-el-Hak 2003; Monkewitz, Chauhan & Nagib 2008). Given that the intent of this paper is to concisely report new high-Reynolds-number TBL profile results, exhaustive tests of the many recent ideas are not pursued. Instead, inner and outer profile fits, based on the zero-pressure-gradient (ZPG) TBL profile forms reported in Monkewitz, Chauhan & Nagib (2007) are provided. In addition, the measured velocity profile data are tabulated in dimensional form in the Appendix.

The prior studies most relevant to the one reported here fall into two groups: smooth-wall laboratory investigations (Fernholz *et al.* 1995; Österlund *et al.* 1999; DeGraaff & Eaton 2000; Knoblock & Fernholtz 2002; Nagib, Christophorou & Monkewitz 2004), where Re_θ reaches or exceeds 10^4 (or Re_x reaches $\sim 10^7$), and the rough-wall atmospheric and wind-tunnel-sidewall boundary-layer experiments (Saddoughi & Veeravalli 1994; Metzger & Klewicki 2001; Metzger *et al.* 2001; Kunkel & Marusic 2006) at much higher Reynolds numbers. The experimental results from the present study extend the Reynolds-number range of the laboratory results to partially close the Reynolds-number gap between the two groups of prior studies.

The experimental results reported here were obtained during a multimonth experimental effort in the fall of 2004. Measurements were made at nominal free-stream flow speeds from 3 to $20 \, \text{m s}^{-1}$ over a 12.9 m long flat-plate test model with a hydraulically smooth test surface mounted in the world's largest low-turbulence water tunnel, the US Navy's William B. Morgan Large Cavitation Channel (LCC). The primary purpose of these tests was to evaluate the skin friction drag reduction induced by injected polymer solutions at high-Reynolds numbers and large scales (Winkel *et al.* 2009). The measurements reported here document the baseline TBL flow on the model without polymer present and include static pressures from test section sidewall taps, average skin friction from flush-mounted floating-plate force balances, and average streamwise velocity from laser Doppler velocimetry (LDV) and near-wall particle tracking velocimetry (PTV). In particular, the static pressure measurements document a mild favourable pressure gradient that leads to a free-stream flow speed increase of approximately 2.5 % over the model's test surface. This pressure gradient is consistent with boundary-layer growth on the model and the LCC test section walls. Thus, the TBL profiles reported here are similar, but not identical, to ZPG TBL profiles.

The remainder of this paper is organized into three sections. The next section describes the experimental set-up, measurement techniques and data processing. The third section presents the profile fitting objective and procedure, the average streamwise velocity profile results, the final parameters for the inner and outer TBL fits and comparisons with the inner and outer ZPG TBL profile fits. This research
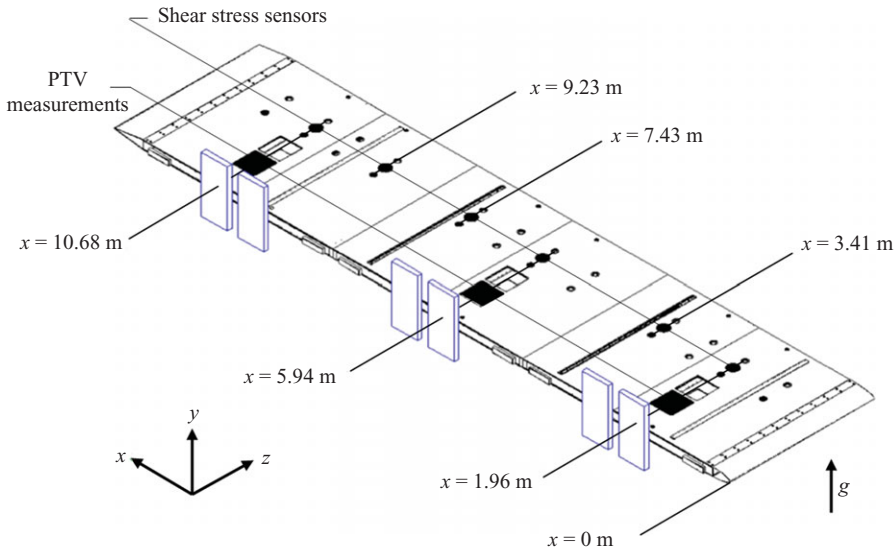
FIGURE 1. (Colour online) Schematic of the test model showing the test surface, instrumentation locations, coordinate system and six water tunnel windows. The model was inverted during the tests so gravity points upwards in this schematic.

effort is summarized and the conclusions drawn from it are stated in the final section. The Appendix provides tabulations of the experimental data in dimensional form.

2. Experimental techniques

The experiments were conducted in the US Navy's William B. Morgan LCC. The LCC's test section has a nominal length of 13 m and a cross-section of $3.05\,\text{m} \times 3.05\,\text{m}$. The LCC may be operated at steady empty test section flow speeds from 0.5 to more than $18\,\text{m\,s}^{-1}$ and at absolute test section pressures from 3.4 to 414 kPa. At the flow speeds of these tests, the LCC's test section centreline turbulence level was 0.2 to 0.4 %. Further description of this facility is available in Etter *et al.* (2005).

The test model was a flat plate with a rounded nose and a tapered trailing edge, as previously described in Sanders *et al.* (2006), Elbing *et al.* (2008) and Winkel *et al.* (2009). It spanned the LCC test section (see figure 1), was 12.9 m long and 18.4 cm thick and weighed 17 metric tons. With these dimensions, test section blockage ($\sim$6 %) produced flow speeds above the developing boundary layer as high as $20.2\,\text{m\,s}^{-1}$ at the primary measurement location. An inflatable model-to-LCC-sidewall seal was used to prevent bypass flow between the top and bottom sides of the model. Additionally, 45° triangular-wedge fillet edge-fairings (75 mm maximum height and width) were installed at the test model-sidewall junction to minimize cavitation, and streamwise junction vortices. The leading edge of the model was a 4-to-1 ellipse while the trailing edge was a 15° full-angle triangular wedge of 0.6 m length that was terminated at 25 mm thickness with 40° bevel angle. This asymmetric trailing edge design was intended to prevent near-wake vortex shedding and its propensity for flow-induced model vibration. The experimental coordinates are shown in figure 1; x is zero at the model's leading edge and increases downstream, y is zero on the test surface and increases perpendicular to it, while z runs in the spanwise direction completing a right-handed Cartesian system.

During testing, surface-normal acceleration was measured with six internally mounted Wilcoxin 754-1 accelerometers. When integrated, these signals produced a maximum measured root-mean-square (r.m.s.) surface-normal vibration velocity of $\sim 0.002 \, \mathrm{m \, s^{-1}}$ at the highest test speed. This vibration fluctuation level was an order of magnitude smaller than the velocity resolution of the LDV system (see below) and was also well below the r.m.s. free-stream velocity fluctuation. Thus, model vibration was negligible in these experiments.

The boundary layer was tripped by an intentional spanwise strip of distributed roughness applied to the elliptical portion of the model starting 25 mm from the model's leading edge and extending 250 mm downstream. The distributed roughness was composed of nominally 120 μm diameter sand grains (100 grit) embedded in a film of epoxy and spaced randomly 2–5 mm apart. The design of this distributed roughness trip was based on guidelines provided by Professor H. Nagib (private communication 2002). Otherwise, the model was hydraulically smooth from its leading edge to the trailing edge wedge, except for the injector opening at $x = 1.32 \, \mathrm{m}$. The test surface was 304 stainless steel polished to a nominal surface roughness of $k = 0.4 \, \mu\mathrm{m}$ or less.

The ratio, $k^+ = k/l_v$, was less than or equal to 0.2 over the entire test surface for all flow conditions. The water temperature, $21.2 \pm 3.5 \, ^{\circ}\mathrm{C}$, varied during the experiments. Water density (ρ), and dynamic (μ) and kinematic (ν) viscosities at the average temperature $21.2 \, ^{\circ}\mathrm{C}$ are $\rho = 998 \, \mathrm{kg \, m^{-3}}$, $\mu = 0.973 \times 10^{-3} \, \mathrm{kg \, m^{-1} \, s^{-1}}$ and $\nu = 9.75 \times 10^{-7} \, \mathrm{m^2 \, s^{-1}}$, respectively, and these values were used for data reduction and in the various normalizations.

Static pressure, $P(x)$, was measured at 11 downstream (x) locations with a Rosemount 3051P transducer and 1.6 mm diameter taps located at $y = 48.3 \, \mathrm{cm}$ on the sidewalls of the LCC test section. This transducer was calibrated with a Druck DP601 pressure source and a Paroscientific DigiQuartz Model 740 pressure transducer. Static pressure measurements were corrected for zero-bias (or drift) error via no-flow pressure measurements performed before and after TBL data acquisition. Static pressure measurements are reported here in terms of the pressure coefficient, $C_p(x) = (P(x) - P_1)/\frac{1}{2}\rho U_\infty^2$, where P_1 is the pressure measured at the first tap at $x = 1.96 \, \mathrm{m}$ and U_∞ is the nominal free-stream flow speed over the geometric centre of the test surface; $U_\infty = 6.7$, 13.2 and $19.9 \, \mathrm{m \, s^{-1}}$ at the three primary test speeds. Hole error (see Benedict 1984) leads to a minimum C_P-uncertainty of ± 0.0005.

Average skin friction, $\tau_w(x)$, on the test surface was measured throughout the multimonth test period with six floating-element strain gauge force balances located at $\sim 1/3$ span and at $x = 1.96$, 3.41, 5.94, 7.43, 9.23 and 10.68 m. The round sensitive surfaces of these balances were 15.24 cm (6 in.) in diameter and were adjusted flush with the test surface. The gap around the sensing surface circumference was at most $\sim 7.5 \, \mu\mathrm{m}$, and was checked for uniformity (and minimum clearance) using 51 μm (0.002 in) stainless steel feeler gauges. For these experiments, the minimum wall unit l_v was 1.7 μm, hence the worst-case average and maximum circumferential gaps were $30 l_v$ and $44 l_v$ respectively.

Strain gauge amplifiers (Vishay 2310) were employed for excitation, nulling and amplification of the skin friction signals. The amplified signals were low-pass filtered at 10 Hz and sampled at 50 Hz. Measured skin friction forces were determined primarily from 10 s (or longer) averages. The force balances were calibrated individually using a suction cup on the floating plate attached via a wire rope to a second precision load cell (Omega LCEB-5) mounted on a finely adjustable translation stage. The force balances were calibrated by temporarily fixing the base of the translation

stage and then adjusting the wire rope's tension with horizontal movement of the precision load cell to produce known and repeatable horizontal loads. A linear fit to the calibration data was used to convert measured voltages to horizontal force; the root-mean-square deviation of the calibration points from linear fits corresponded to at most ± 0.02 N. These skin friction measurements are reported here in terms of the skin friction coefficient, $C_f(x) = \tau_w(x)/\frac{1}{2}\rho U_e^2(x)$, where $U_e(x)$ is the local free-stream speed.

For the skin friction measurements, the significant sources of uncertainty included drift and calibration errors. To decrease the influence of drift, the strain gauge bridges were nulled during periods of no flow every 1 or 2 h during a test day. For any particular 10 s average skin friction measurement, the error associated with drift was approximately 1–2 %, and this percentage was independent of flow speed. To combat drift error, the numerical average of at least 12 independent 10 s measurements for the same flow condition is reported and the drift uncertainty, σ_{drift}, is taken to be twice the standard deviation of the mean of these 12 (or more) measurements. The uncertainty associated with calibration, σ_{cal}, is taken to be twice the standard deviation of the mean of multiple calibrations (also typically 1–2 %) recorded over a period of several days or more. The combined experimental uncertainty, $\sigma = \sqrt{\sigma_{drift}^2 + \sigma_{cal}^2}$, varied somewhat between force balances, but was always less than ± 4 % of the final skin friction measurement from any particular force balance for $U_e \geqslant 6.7 \, \mathrm{m \, s^{-1}}$.

Fluid velocity measurements were made with two LDV systems. The first was fixed in place and used to monitor the test section inlet streamwise velocity at $x = -6.2$ cm and $y = 14.1$ cm. It operated with a $2.775 \times$ beam expander, 115 mm beam spacing and 800 mm focal length. The second was mounted on a precision traverse and was used for measuring the mean streamwise velocity component, $U(x, y)$, in a pair of vertical columns ($0.1 \, \mathrm{mm} < y \leqslant 300 \, \mathrm{mm}$) near $x = 10.7$ m. This system consisted of Dantec BSA 57N11 signal processors, fibre optic probes, a Spectra Physics 6-W Argon-Ion laser (model 2017), a Dantec three-dimensional traverse and Dantec Flow software. This system was operated at 514.5 and 488 nm wavelengths with a $1.5 \times$ beam expander, 112 mm beam spacing and 1600 mm focal length. The burst processor parameters included transit-time-weighted averages for velocity bias correction, low and high-pass filtering dependent on free-stream velocity and particle size rejection for the elimination of erroneous measurements from reflections off the polished test surface. The y-coordinate origin for the second LDV system was determined to ± 0.1 mm by measuring the near-wall fluid velocity with the LDV beams above, coincident and reflecting from the model's working surface, and setting $y = 0$ at the location of minimum average streamwise velocity.

For the LDV measurements, the water channel was flood-seeded with silicon carbide particles with a nominal diameter of $3 \, \mu\mathrm{m}$. The traversing LDV system had a prolate focal volume with a diameter of $170 \, \mu\mathrm{m}$ and a length of 6.5 mm that was oriented with its long axis perpendicular to the flow direction but nearly parallel to the plate surface. To make measurements near the test surface, the LDV's head was tilted $2.2°$, and this increased the projected vertical dimension of the downstream LDV focal volume to $250 \, \mu\mathrm{m}$. In addition, the LDV head tilt led to non-normal optical transmission at the vertical LCC sidewall windows. The resulting optical distortion and reduction in data rate limited the LDV focal volume's spanwise distance from the LCC sidewall to 0.65 m. However, this spanwise location is well beyond the furthest influence of the test-model-sidewall junction flow (~ 0.20 m from the LCC sidewall).
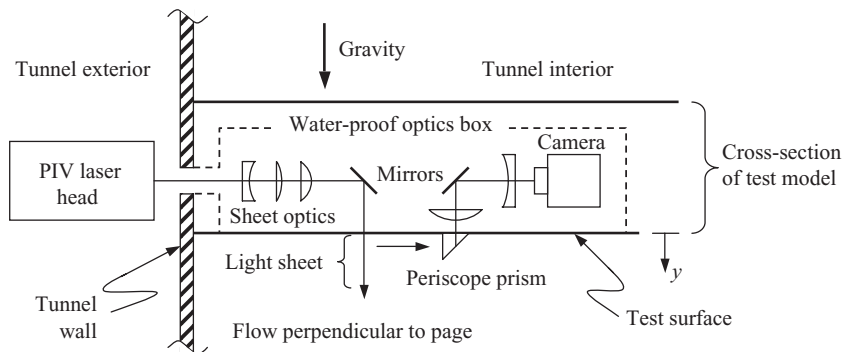
FIGURE 2. Cross-section schematic of the near-wall PTV set-up. The illumination light pulses originate in a double-cavity Nd-YAG PIV laser head that is mounted to the outside wall of the water tunnel. Sheet-forming optics and a 45° mirror inside a waterproof optics box fan the light into a sheet that is parallel to the flow direction and perpendicular to the test surface. Side-scattered light from the sheet is directed via a periscope prism and another 45° mirror to a digital camera after passing through two cylindrical lenses (focal lengths: +75 mm, and −300 mm) to provide anisotropic, preferential magnification in the y-direction.

Both LDV systems were calibrated with a spinning disk covered with 60 grit emery paper that was driven by a CompuMotor Model SM233BE-NTQN and CompuMotor TQ10X Servo-Controller. The major contributor to the uncertainty of the calibration is the ± 0.4 r.p.s. accuracy of the motor as listed by its manufacturer. The LDV calibration data scatter about a linear fit was less than $\pm 0.005\,\mathrm{m\,s^{-1}}$. The overall LDV velocity uncertainty for the traversing system was $\pm 0.025\,\mathrm{m\,s^{-1}}$ at the 95 % confidence level (Park, Cutbirth & Brewer 2003).

A total of six LDV-measured profiles are reported in the next section. They were measured at $x = 10.555$ and 10.795 m, and had nominal free-stream flow speeds of 6.7, 13 and 20 m s^{-1}. The average streamwise velocity at each point of the six nominally-50-point profiles was determined from 10 000 LDV bursts. The burst processor's gain and photomultiplier tube voltage were adjusted for each measurement location so that the burst rate remained relatively constant, 100–170 Hz, with respect to the distance from the plate.

Unfortunately, the size of the two-component LDV focal volume prevented its use for near-wall velocimetry (i.e. for y^+ less than 100 or so). Thus, to complete the flow profile measurements, a custom-designed near-wall PTV system was assembled in a watertight box that was built into the test model at $x = 10.68$ m. The PTV system design is shown in figure 2, which schematically depicts the laser source, camera and optical pathways. Here, the near-wall flow was imaged through a periscope prism that protruded into the flow. The imaged region was preferentially (anisotropically) magnified in the wall-normal direction by using a cylindrical lens combination to produce a nominal threefold vertical stretching and a 2 mm vertical field of view. The geometrical and hydrodynamic design of the prism were modelled after the periscope–mirror LDV work of Compton & Eaton (1996, 1997). The prism protruded 5 mm from the test surface and was $\Delta z = 5$ cm from the laser light sheet. This receiving-side optical train design eliminated the need for large focal length tunnel exterior optics, and allowed particle reflections from the test surface to be imaged and subsequently used to accurately locate the wall in the PTV images. The dual-cavity, double-pulsed Nd-YAG laser (New Wave Solo 50 mJ) was bolted tightly to the exterior side of the LCC to minimize relative motion between the lasers and the illumination path optics. The laser's green beam (532 nm) was relayed from the exterior of the tunnel through a

straight 40 mm diameter watertight conduit to sheet-making optics in the test-model-interior watertight box, and then reflected into the flow via a 45° laser mirror to form a light sheet lying in an x,y-plane having a thickness of $75 \pm 25\,\mu m$. The sheet thickness was measured directly by passing the beam at the measurement location through a graded microscope objective lens and expanding it upon its exit from the eyepiece onto a white screen. The PTV camera was fitted with a Nikon 105 mm/f 2.8 micro-Nikkor lens attached to two Nikon TC-201 teleconverters (2× each). Spatial calibration of the resulting images was accomplished by imaging a precision test target placed in the PTV interrogation plane that was composed of a square array of $20\,\mu m$ round dots with centre-to-centre spacing of $50 \pm 0.02\,\mu m$. The resolution of the cross-correlation charge-coupled device (CCD) camera was 1024×1280 pixels (LaVision FlowMaster CCD camera) and the camera was oriented to utilize its higher resolution in the wall-normal direction. The final x,y frame size was $4.78\,mm \times 2.01\,mm$. Thus, a camera pixel corresponded to a rectangle $5\,\mu m$ in the x-direction and $1.6\,\mu m$ in the y-direction.

The PTV particles were titanium dioxide with a nominal size of $1\,\mu m$ and specific gravity 4.26 from J.T. Baker Industries. Adding 7–10 kg of TiO_2 powder flood-seeded the LCC so that approximately five particles appeared in a 32×32 pixel region of the resulting images. A single particle's image was typically elliptical and covered an area of 5×13 pixels.

The PTV laser, camera and data recording were controlled by a PC running DaVis 7.1 software by LaVision Inc. For the investigated flow speeds, the time separation between laser pulses, Δt, varied from 5.5 to $35\,\mu s$ with uncertainty less than 50 ns. Typical particle displacements were 12–16 pixels in the mean flow direction. At the actual data rate of 4–12 dual frames s^{-1}, any PTV frame pair was uncorrelated temporally from the preceding or following pair. A minimum of 3500 frame pairs was recorded at each flow condition.

The PTV processing involved a series of steps that converted elongated (elliptical) particle images to average velocity profiles. First, the test surface reflection was used to determine the wall location within each instantaneous PTV frame with an accuracy of better than ± 1 pixel. This was done via a two-dimensional cross-correlation computation between the imaged particles and their reflections. Frame-to-frame variation in this reflection-determined wall location lead to random errors of the order of one wall unit in the vertical location of particle images. Next, the x,y-coordinates of the centroid of individual particle images were located to ± 0.1 pixel with a two-dimensional spatial matched-filter search of each frame. This filtering step allowed particle image centres to be reliably located within one pixel of the wall even though the actual particle image sizes were much larger and overlapped the wall location in the recorded frames. The matched-filter-determined particle-image-centroid locations were converted back to physical x,y-coordinates using the calibration frame information. This pixels-to-spatial-coordinates calibration was the source of the greatest uncertainty in the PTV mean velocity measurements, and was thought to be less reliable than the LDV calibration. Thus, the PTV-determined velocities reported in the next section have been multiplied by 1.02 so that they match the LDV-determined velocities where the measurements overlap. This correction factor has not been applied to the tabulated data in the Appendix.

Once all particle-image-centroid locations were determined for a PTV frame pair, linking first- and second-frame images for the same particle was accomplished by selecting a first-frame particle image and then searching a spatial window in the second frame where this particle's second image was expected to appear. If no particles were found in the second-frame search window, the first-frame particle was discarded. If

one or more particle images were found in the second-frame search window, then two concurrent tests were conducted to determine the highest probability match. First, a two-dimensional cross-correlation value was computed between the particle intensity distribution in the first frame and all possible particle images in the second frame. This correlation window was 24×24 pixels centred at the particle images' centroidal pixels. The second-frame image with the highest cross-correlation value was presumed most likely to be the correct match to the first-frame particle. The second test involved checking whether the highest computed correlation value was an actual correlation peak, by repeating the correlation calculation eight times corresponding to eight different test shifts of the first 24^2 pixel box around the second-frame particle image centroid. If the correlation value without a test shift was higher than that for any of the eight test shifts, then the image was considered the correct match for the particle in the first frame and the particle's (x, y)-velocity (u, v) was determined simply from the particle's centroid displacement divided by the time between frames, Δt. This process was repeated for all possible first-frame particle images. At the end of this process, each frame pair produced an instantaneous velocity field that was randomly sampled in space. Unfortunately, this processing scheme may under-sample particles having a non-zero laser-sheet-normal velocity component. However, given that the expected value of such spanwise velocity fluctuations is zero and that the variance of these spanwise fluctuations is typically small compared to U^2, no correction was attempted to counter this possible particle sampling bias.

After this conversion from particle images to velocity vector samples, a post-processing filter was implemented on each instantaneous field to eliminate spurious vectors. The filter compared the vertical and horizontal components of the vector under consideration with the mean and r.m.s. components of all the vectors within a radius of 80 pixels and spurious vectors were removed. For the reported data, the spurious vector percentage ranged between 4 and 7%. These filtered instantaneous velocity field results were then averaged in the streamwise direction and across all frame pairs from the same experimental run by sorting the instantaneous velocity vectors into bins centred at selected y-locations. Small bins (1–4 pixels) were chosen close to the wall to resolve the near-wall flow, while farther from the surface, $y^+ > 50$, larger bins (16 pixels) were used. Once compiled, there were typically 10^4 vector samples in the small bins nearest the wall, and 5×10^4 vector samples in the larger bins farther from the wall. Averages for each bin were computed directly from the vector samples in that bin and reported at the bin-centre vertical location.

For PTV to be successful, the second-frame search window size and shape need to be optimized so that appropriate second-frame particle images are found reliably. Here, a power-law second-frame search window was used with horizontal and vertical sizes that expanded linearly and quadratically, respectively with increasing y from $y^+ = 0$ to 17; the search window size was constant for larger y. At the y-location of each bin, the second-frame search window was sufficient to capture the mean and ± 3 standard deviations of the measured particle motion.

Figure 3 illustrates the PTV processing method in scaled physical coordinates (x^+, y^+) where the flow is from left to right. Figure 3(*a*) shows first-frame particle images, with the matched-filter-identified particle images marked at their centroids. The diagonal extent of the particle images is a remnant of minor misalignment in the PTV system collection optics. Figure 3(*b*) shows the identified first-frame particle centroids from figure 3(*a*) along with their second-frame search windows. Here, the identified second-frame particles are shown along with a line segment connecting the first- and second-frame particle image centroids when the image pair led to a valid
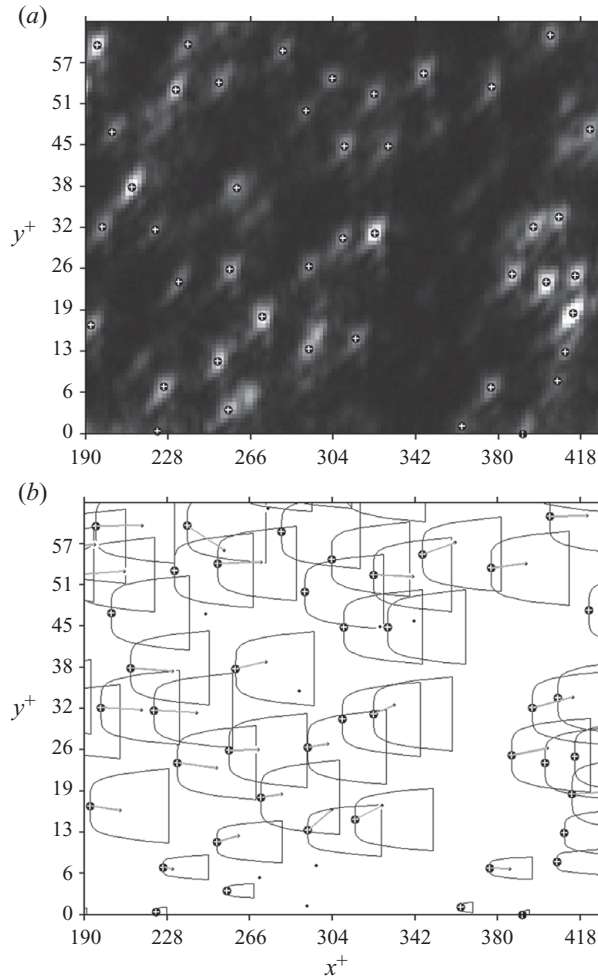
FIGURE 3. Sample PTV processing information. (*a*) First-frame particle images with the matched-filter-identified particle centroids marked with a white cross in a black circle. The wall is located at $y^+ = 0$ and the flow is from left to right. The frame is 125 pixels in the x-direction by 100 pixels in the y-direction. (*b*) A composite drawing superimposing the second-frame matched-filter-identified particle image centers (black dots), the particle image locations from the first frame (white cross in a black circle), search envelopes and PTV-determined velocity samples (line segments).

velocity vector sample. These line segments represent velocity samples from the PTV measurements. Variations in the second-frame search window size of 30 % produced no noticeable change in the final PTV-determined values of average streamwise velocity.

Figure 4 shows a sample composite velocity profile for $Re_\theta = 156\,000$. The LDV and corrected PTV measurements are plotted as diamonds and circles, respectively.

3. Average results

3.1. *Static pressure*

The dependence of the static pressure in the LCC test section on the streamwise coordinate x is shown in figure 5 in terms of the pressure coefficient, $C_P(x)$.
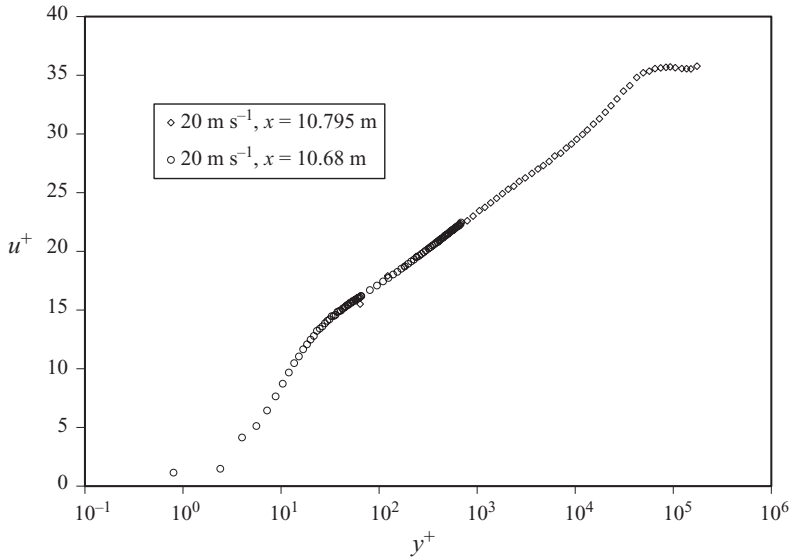
FIGURE 4. Composite velocity profile measurements for $Re_\theta = 156\,000$ using the classical TBL scalings: $U^+ = U/\sqrt{\tau_w/\rho}$, and $y^+ = y(\sqrt{\tau_w/\rho})/\nu$. Here, the measurements extend over nearly six orders of magnitude in y^+. The corrected PTV data appear as circles, and the LDV data appear as diamonds.
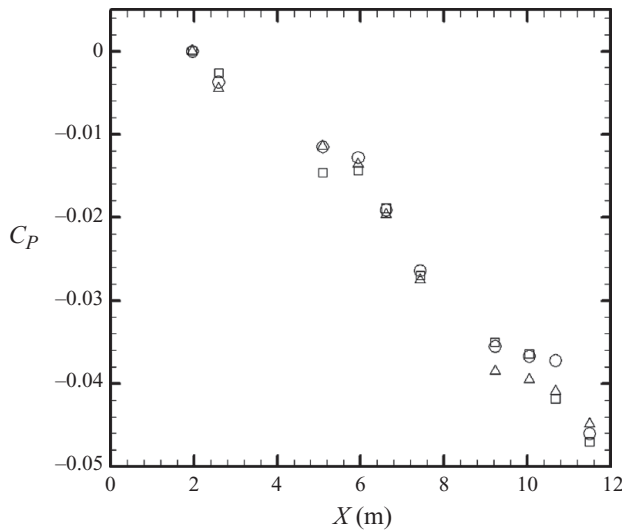
FIGURE 5. Static pressure coefficient, $C_p(x) = (P(x) - P_1)/\frac{1}{2}\rho U_\infty^2$, versus distance from the leading edge of the test model, x (in m), for test model centre flows speeds: $U_\infty = 6.7\,\mathrm{m\,s}^{-1}$ $\square$, $13.2\,\mathrm{m\,s}^{-1}$ $\bigcirc$ and $19.9\,\mathrm{m\,s}^{-1}$ $\triangle$. Here, P_1 is the static pressure measured at the first tap at $x = 1.96\,\mathrm{m}$. The favourable pressure gradient is consistent with boundary-layer growth on the model and the LCC test section sidewalls.

Downstream of the test model's elliptical leading edge, the tunnel and test-model cross-sections were geometrically constant for more than 10 m. The mild favourable pressure gradient is consistent with boundary-layer growth on the test model and the LCC-test-section sidewalls. For the profile fitting, the free-stream velocity change, ΔU_e, over a relatively small change in downstream distance, Δx, can be estimated

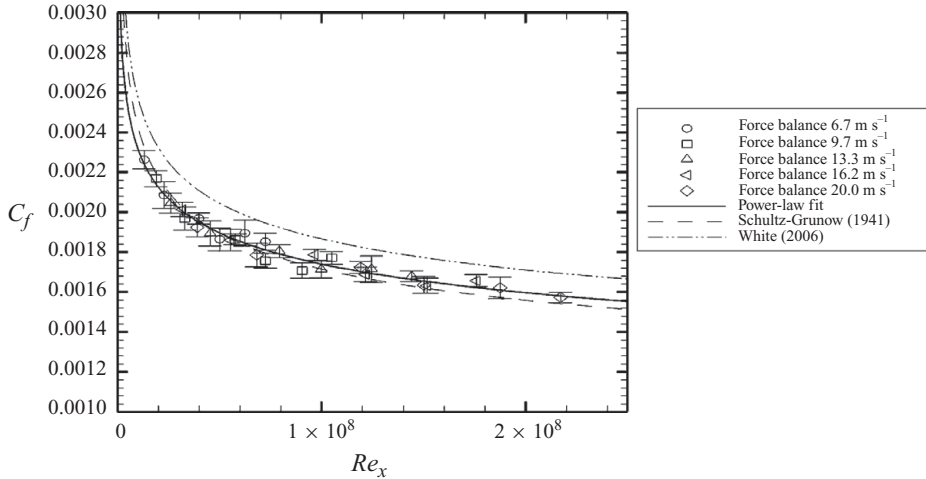FIGURE 6. Skin friction coefficient, $C_f = \tau_w / \frac{1}{2}\rho U_\infty^2$, versus $Re_x = U_e x/\nu$ from the flush-mounted floating-plate force balances. The solid curve is a power-law fit to these measurements. The two dashed lines are classic friction correlations, and are plotted merely for reference.

from the usual Bernoulli equation and the first derivative of the definition of $C_P(x)$

$$\Delta U_e \approx \frac{U_\infty^2}{2U_e} \frac{\mathrm{d}C_p}{\mathrm{d}x} \Delta x. \tag{3.1}$$

At the TBL profile measurement location, $x = 10.7\,\mathrm{m}$, the measurements are somewhat more scattered than elsewhere and $\mathrm{d}C_P/\mathrm{d}x = 0.006 \pm 0.003\,\mathrm{m}^{-1}$.

3.2. *Average skin friction*

The downstream variation of the average skin friction is shown in figure 6 in terms of the skin friction coefficient, C_f, and the downstream-distance-based Reynolds number, $Re_x = U_e x/\nu$. Results from $1.96\,\mathrm{m} \leqslant x \leqslant 10.68\,\mathrm{m}$, and $U_e = 6.6$–$20.2\,\mathrm{m\,s^{-1}}$ are plotted along with error bars representing the 95 % confidence interval. The solid line is a least-squares power-law fit

$$C_f = (0.0170 \pm 0.004)Re_x^{-(0.1237 \pm 0.0067)} \tag{3.2}$$

that matches these measurements to within experimental uncertainty. The empirical constants in this power-law fit implicitly include the influence of flow artifacts arising from the test model's elliptical leading edge, the boundary layer trip and the uncovered injector opening used in other experiments. In addition, there may be Re-dependent variation in the TBL's virtual origin. Yet, such influences may be small. Together, the curved portion of the test model's leading edge and the distributed roughness trip occupy the first 0.37 m of the test model, only 3.5 % of the wetted length (10.8 m) of the experiment and the profile measurement locations are more than 9 m downstream from the injector opening. While correlations with Re_x are desirable and convenient for practical applications, they are of limited value for scientific study of TBLs. A more robust skin friction correlation based on TBL displacement or momentum thicknesses would be preferable to (3.2); however, production of such a correlation was not possible because TBL profile measurements were made at only a few of the many test conditions where wall shear stress was measured. The dashed curves on figure 6, which are plotted for reference, are the classical skin friction correlations of Schultz–Grunow (1941) and White (2006).

3.3. *Velocity profile fitting and results*

Following classical TBL scaling, as described in Marusic *et al.* (2010), the six measured velocity profiles were fit to empirical forms for the TBL's inner (viscous) and outer (inviscid wake-like) regions. Adjusted versions of the ZPG TBL profile forms suggested in Monkewitz *et al.* (2007) were used for this fitting task and are described in the following two paragraphs. These profile forms were chosen because they cover the entire wall-normal range of the current measurements, they provide a natural means for comparisons with ZPG TBL results and they are sufficiently flexible to fit the not-quite-ZPG profiles presented here. The primary purposes of this fitting exercise were to mitigate the influence of the experimental uncertainties and statistical limitations of the data when deducing TBL parameters, and to determine if one inner profile form and one outer profile form would provide a satisfactory fit to the data at all three Reynolds numbers while conserving streamwise momentum. A secondary purpose was to determine how closely the resulting inner and outer fits were to recent ZPG TBL results.

The inner fit, valid from $y^+ = 0$ to y^+ of several thousand, is determined from the scaled wall-normal mean-streamwise-velocity gradient and two Padé approximants:

$$\frac{\mathrm{d}U^+_{inner}}{\mathrm{d}y^+} = b_0 \frac{1 + b_1 y^+ + b_2 y^{+2}}{1 + b_1 y^+ + b_2 y^{+2} + \kappa b_0 b_2 y^{+3}}$$
$$+ (1 - b_0) \frac{1 + h_1 y^+ + h_2 y^{+2}}{1 + h_1 y^+ + h_2 y^{+2} + h_3 y^{+3} + h_4 y^{+4} + h_5 y^{+5}}, \quad (3.3)$$

where $U^+ = U/\sqrt{\tau_w/\rho}$ as usual, κ is the von Kármán constant, and the b values and h values are fitting constants. After integration, (3.3) produces the familiar viscous-sublayer $U^+ = y^+$ for $y^+ \to 0$, and the classical logarithmic law $U^+ = (1/\kappa)\ln(y^+) + B$ for $y^+ \to \infty$. While (3.3) incorporates κ directly, it only produces the intercept parameter, B, after integration. So, to develop the inner profile fits reported here, (3.3) was numerically integrated from the initial condition $U^+ = y^+ = 0$, and a single set of the fitting constants was chosen by trial-and-error to match the corrected PTV data with minimal alterations from the ZPG TBL fitting constant values recommended in Monkewitz *et al.* (2007). This approach ensured that the inner profile achieved a logarithmic law form for $y^+ > 10^3$ and facilitated comparisons with ZPG TBL results.

The outer fit used here is valid for y^+ above a thousand or so, and is defined by

$$U^+_{outer} = U^+_e - \left[\frac{1}{\kappa} E_1(\eta) + w_0\right] \frac{1}{2} \left[1 - \tanh\left(\frac{w_{-1}}{\eta} + w_2 \eta^2 + w_8 \eta^8\right)\right], \quad (3.4)$$

where $E_1(\eta) = \int_\eta^\infty (e^{-t}/t)\,\mathrm{d}t$ is the exponential integral, $\eta = y/(U^+_e \delta^*)$ is the Rotta–Clauser outer flow similarity parameter, δ^* is the TBL's displacement thickness, and the w values are fitting constants. Here again, the fitting function incorporates κ directly, but this time the log law is recovered for $\eta \to 0$, while the Coles–Fernholz relation (Fernholz & Findley 1996) determines the logarithmic-law intercept parameter

$$B = U^+_e - \frac{1}{\kappa}\left[\ln\left(\frac{U^+_e \delta^*}{l_v}\right) - \gamma\right] - w_0, \quad (3.5)$$

where $\gamma = 0.57721566$ is the Euler constant. The outer profile fits reported here were obtained by a constrained trial-and-error search of the available parameter space. In practice, this meant cyclically repeating the following steps: (i) select fit input values for κ, U^+_e, δ^*, and the w values, (ii) compute a trial profile from (3.4) using the measured τ_w and the average temperature values of ρ and μ, (iii) assess how well the constraints

Constant	Current fit	ZPG	Range considered
κ	0.380 ± 0.002	0.384	0.378–0.384
B	5.147 ± 0.002	4.17	4.17–5.50
b_0	$0.01/\kappa$	$0.01/\kappa$	$(0.009\text{--}0.0105)/\kappa$
b_1	0.01	0.011	0.008–0.012
b_2	0.92×10^{-4}	1.1×10^{-4}	$(0.7\text{--}1.2) \times 10^{-4}$
h_1	-0.01	-0.01	-0.02 to $+0.05$
h_2	0.011	0.006	0.005–0.012
h_3	1.0×10^{-3}	0.9977×10^{-3}	$(0.7\text{--}1.2) \times 10^{-3}$
h_4	2.2×10^{-5}	2.2×10^{-5}	$(1.0\text{--}3.0) \times 10^{-5}$
h_5	2.3×10^{-6}	1×10^{-6}	$(0.9\text{--}3.0) \times 10^{-6}$
w_{-1}	-0.096	-0.096	$-$
w_0	-0.03	0.6332	-0.05 to 0.6
w_2	17.4	28.5	15–30
w_8	10^4	3.3×10^4	$(0.8\text{--}3.3) \times 10^4$

TABLE 1. Fit constants.

were satisfied and (iv) return to step (i) if a better fit is likely with adjusted input parameters. Throughout this process, slightly larger data-fit differences were allowed at $6.7\,\mathrm{m\,s^{-1}}$ because the relative uncertainty in the shear stress and static pressure measurements was larger at this free-stream flow speed when compared to 13 and $20\,\mathrm{m\,s^{-1}}$.

The five constraints considered during the outer profile fitting procedure were: (i) all the fitted profiles must have the same values for κ, B, and the w values; (ii) the difference between the fitted and measured profiles must be small and uniformly distributed for $y^+ > 10^2$; (iii) the input value of δ^* must match the fit-determined value of δ^* for each profile; (iv) the fitted profile pairs at each Reynolds number must satisfy the von Kármán momentum integral equation and (v) the U_e^+ values for each profile pair must be consistent with the measured pressure gradient.

These five profile-fitting constraints were met by repetitively considering each during the trial-and-error fitting procedure. The first constraint was satisfied in the fitting procedure by using the same values for κ, the b values, the h values and the w values for fitting each profile, and then adjusting the input values of U_e^+ and δ^* to recover a common value of B to within 0.002. The second constraint was monitored by examining plots of the data-fit difference as a function of y^+. The third and fifth constraints were assessed simply by comparing the input and fitted-profile-calculated values of δ^* and ΔU_e, where the input values of ΔU_e were obtained from (3.1). The fourth constraint was investigated by comparing the skin friction coefficient C_f determined from (3.2), and from a discretized form of the von Kármán momentum integral equation

$$(C_f)_{x=\bar{x}} \approx \frac{2}{\bar{U}_e^2} \frac{\left(U_{e2}^2 \theta_2 - U_{e1}^2 \theta_1\right)}{x_2 - x_1} + \frac{\left(\delta_2^* U_{e2} + \delta_1^* U_{e1}\right)}{\bar{U}_e^2} \frac{\left(U_{e2} - U_{e1}\right)}{x_2 - x_1}, \tag{3.6}$$

where the '1' and '2' subscripts indicate quantities evaluated at $x_1 = 10.555\,\mathrm{m}$ and $x_2 = 10.795\,\mathrm{m}$, respectively, $\bar{x} = (x_1 + x_2)/2$ and $\bar{U}_e = (U_{e1} + U_{e2})/2$. Here, it should be noted that the precision and accuracy of the present data are insufficient for use of (3.6) to predict the skin friction coefficient C_f. Therefore, the final profile fits should be interpreted as being consistent with the independent skin friction measurements reported in figure 6. Although the overall profile fitting procedure lacked mathematical elegance, it was sufficient for the current task.

x (m)	10.555	10.795	10.555	10.795	10.555	10.795
$U_{e,fit}$ (m s^{-1})	6.680	6.689	13.361	13.368	20.199	20.205
ΔU_e (m s^{-1}), (3.1)	0.005		0.009		0.014	
$\Delta U_{e,fit}$ (m s^{-1})	0.009		0.007		0.006	
τ_w (Pa)	41.25	41.13	149.3	148.9	322.6	321.7
$\sqrt{\dfrac{\tau_w}{\rho}}$ (m s^{-1})	0.2033	0.2030	0.3868	0.3862	0.5685	0.5677
$l\nu$ (μm)	4.79	4.80	2.520	2.523	1.714	1.717
δ^*_{input} (mm)	9.85	10.15	9.32	9.55	8.98	9.19
δ^*_{fit} (mm)	9.833	10.132	9.317	9.545	8.991	9.187
θ_{fit} (mm)	7.915	8.099	7.587	7.776	7.344	7.528
$Re_x = U_e x/\nu$	7.3×10^7	7.5×10^7	1.45×10^8	1.48×10^8	2.19×10^8	2.23×10^8
$Re_\theta = U_e \theta/\nu$	5.4×10^4	5.63×10^4	1.04×10^5	1.07×10^5	1.52×10^5	1.56×10^5
C_f, (3.2)	0.001812		0.001665		0.001582	
C_f, (3.6)	0.001800		0.001675		0.001596	

TABLE 2. Physical parameters of the profile fitting.

Tables 1 and 2 list final numerical values for the profile fitting constants and the TBL flow parameters, respectively. In addition, table 1 provides uncertainties for κ and B. The uncertainty in κ is the range of κ over which similar profile fitting results could be obtained. The uncertainty in B is the range of B values from the reported fits of the six LDV profiles. Table 1 also provides a specification for the currently investigated range for each profile constant, and the profile fitting constants from Monkewitz *et al.* (2007) determined from ZPG TBL data spanning $2500 \leqslant Re_\theta \leqslant 70\,000$. The primary differences between the current and ZPG-TBL constants involve the logarithmic-law intercept constant (B and w_0) and the TBL profiles' wake component (w_2 and w_8). The current TBL flow is faster (higher B and lower w_0), and has a smaller wake (lower w_2 and w_8) component than an equivalent ZPG TBL. Both of these observations are consistent with trends found in lower Reynolds-number favourable-pressure-gradient TBL measurements (Bourassa & Thomas 2009). Furthermore, the current κ and B values fall within the scatter of the empirical fit for κ and B determined from a variety of wall-bounded turbulent flows with pressure gradients (Nagib & Chauhan 2008). Yet, the elevated B-value from the current measurements might be an experimental artefact arising from one or more physical details of the test model or water tunnel, imperfect velocimetry, or shear stress calibrations or even background thermal changes. However, it is consistent across all three Reynolds numbers considered here, so it is unlikely to be caused by random error.

Table 2 provides numerical values for the physical parameters of the profile fitting. The third and fourth rows of this table address the fifth fitting constraint by listing the ΔU_e values determined from the fitting and from (3.1). Although the pairs of ΔU_e values for each nominal flow speed are not perfectly matched, they are of the same order of magnitude and are in agreement with each other when the uncertainties of the LDV velocity (± 0.025 m s^{-1}) and pressure coefficient gradient ($\pm 50\,\%$) are considered. The fifth line of table 2 provides shear stress values based on the measurements that have been corrected for the up- and downstream displacement of the measured profile pairs. These values fall within the 95 % confidence interval specified by (3.2). The eighth and ninth rows of table 2 address the third fitting constraint by listing the input and fit-determined values of δ^*. Here, the average and maximum percentage differences are 0.10 and 0.18 %, respectively. The final two rows of table 2 address the
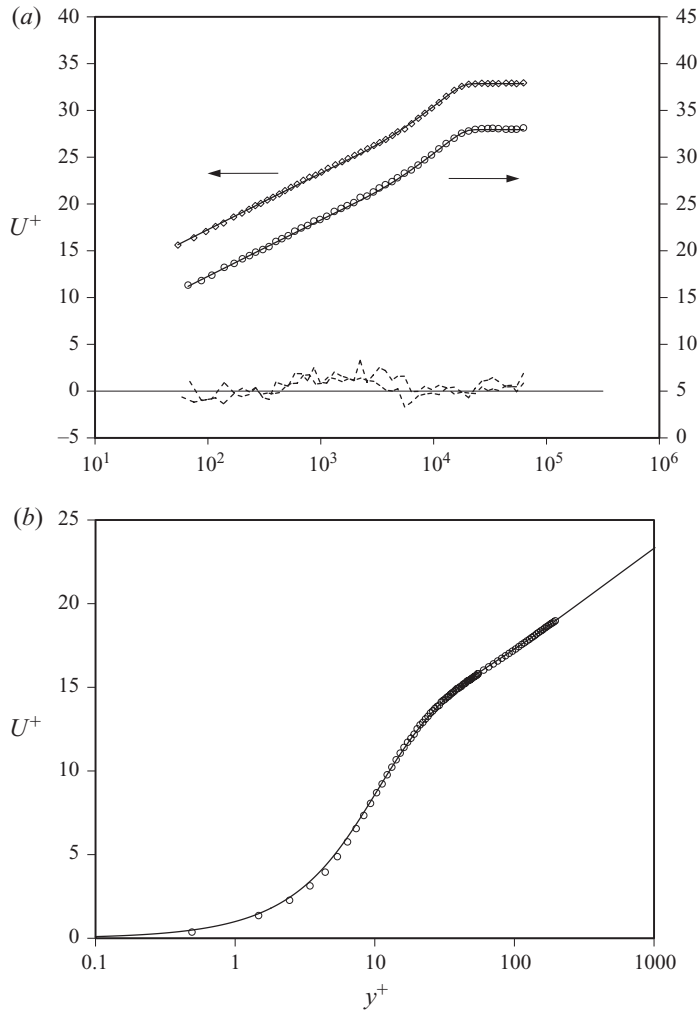
FIGURE 7. Profile fitting results for U^+ versus y^+ at $U_e = 6.7 \, \mathrm{m \, s^{-1}}$: (*a*) LDV data (diamonds) and fitted outer profile (solid line) for $x = 10.555 \, \mathrm{m}$ using the left vertical axis, LDV data (circles) and fitted outer profile (solid line) for $x = 10.795 \, \mathrm{m}$ using the right vertical axis and 10 times the data-fit differences (dashed curves). (*b*) PTV data (circles) multiplied by 1.02 and fitted inner profile (solid line) at $x = 10.68 \, \mathrm{m}$. The multiplier was applied to match the PTV data to the LDV data where the two measurement types overlap.

fourth fitting constraint by listing the C_f values determined from (3.2) and (3.6). The average and maximum percentage differences between C_f pairs are 0.7 and 0.9 %, respectively. The rest of the quantities listed in table 2 are either self-explanatory or are derived from the other table entries.

Figures 7–9 show profile fitting results, U^+ versus y^+, at 6.7, 13 and $20 \, \mathrm{m \, s^{-1}}$, respectively. In each figure, part (*a*) presents the U^+ LDV data, the U^+ outer fit and 10 times the data-outer-fit difference at $x = 10.555 \, \mathrm{m}$ (left vertical axis) and $10.795 \, \mathrm{m}$ (right vertical axis), respectively. Part (*b*) of each figure presents the U^+ PTV data and the U^+ inner fit. For all six outer flow profiles, the r.m.s. difference between the data and the outer fit, $[(1/N)\sum_{i=1}^{N}(U^+_{i,data} - U^+_{i,fit})^2]^{1/2}$, where N is the number of data points in a measured profile, is 0.08–0.13 in U^+ units with the largest value occurring
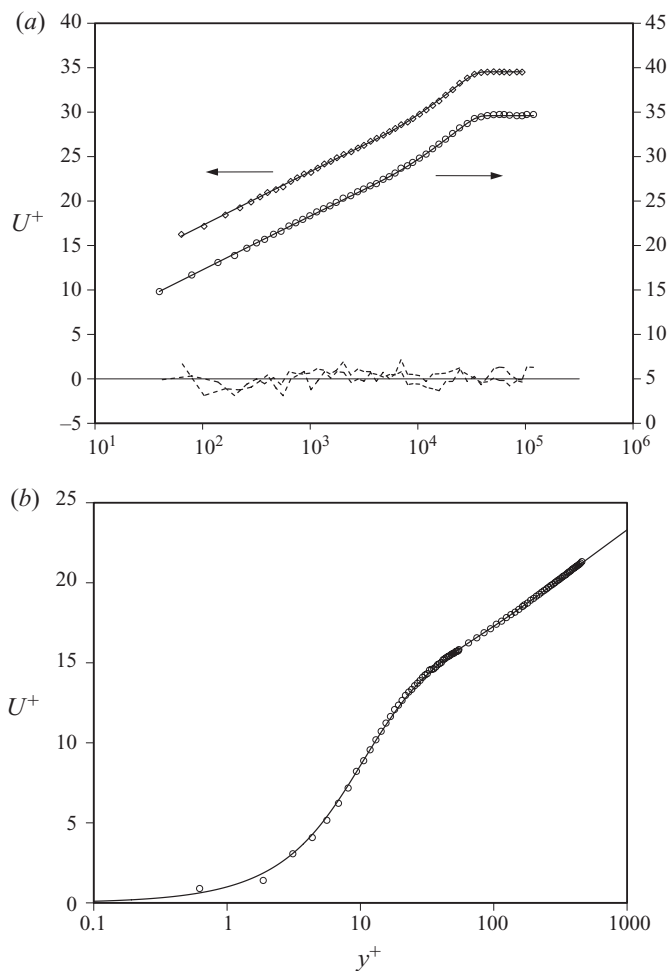
FIGURE 8. Same as figure 7 except $U_e = 13\,\mathrm{m\,s^{-1}}$.

at $6.7\,\mathrm{m\,s^{-1}}$ and $x = 10.795\,\mathrm{m}$ (figure 7(a)). For all six profiles, the bias component of this data-fit difference is approximately two thirds (or less) of the LDV uncertainty ($0.025\,\mathrm{m\,s^{-1}}$); a bias error of this size is consistent with the LDV calibration accuracy. The remaining random (zero-mean) component of this data-fit r.m.s. difference has a standard deviation of 0.2–0.3 % of the local value of U_e and this fluctuation level is comparable to the LCC's turbulence level (0.2–0.4 %). Possible sources of the random component of the r.m.s. data-fit difference (and engineering estimates of the percentage uncertainty they can produce) are: uncompensated temperature variations ($\pm 0.3\,\%$), low-frequency fluctuations in the LCC test section flow speed (as large as $\pm 0.2\,\%$), the statistical limitations of the 10^4-burst LDV data records (as large as $\pm 0.1\,\%$) and localized optical imperfections in the LCC test section window through which the LDV data were collected (perhaps $\pm 0.1\,\%$). Thus, for the outer flow fitting, both the bias and random components of the data-fit differences are less than the relevant experimental uncertainties.

The inner profile fits, shown in part (b) of figures 7–9, are successful for $y^+ \geqslant 10$ and display the same characteristics as near-wall ZPG TBL profiles. For example, the current profile fits include both extrema of the indicator function, $\varXi = y^+(\mathrm{d}U_{inner}^+/\mathrm{d}y^+)$,
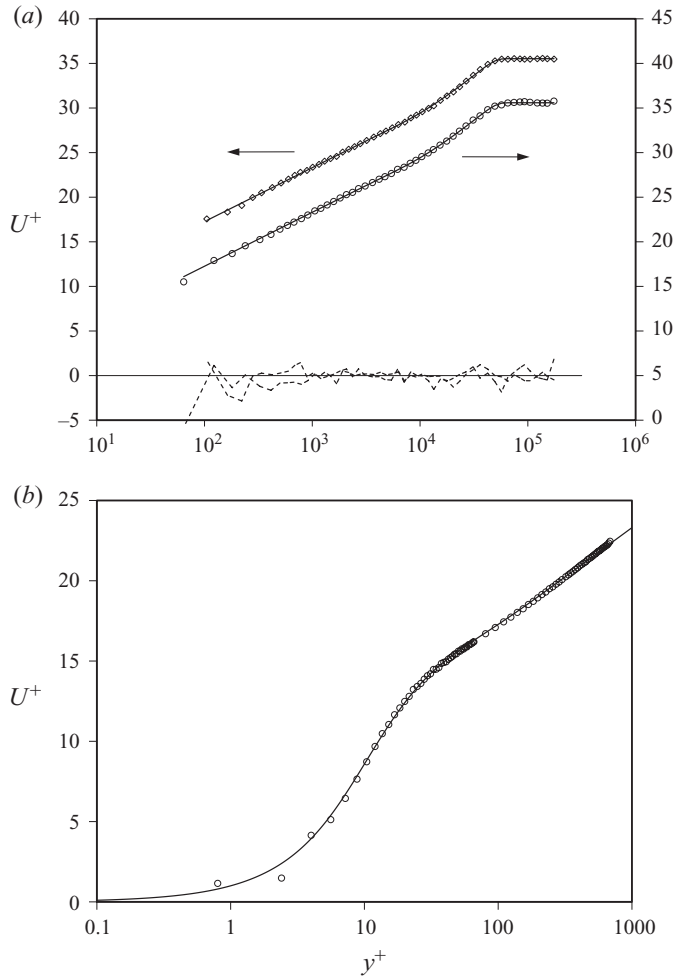
FIGURE 9. Same as figure 7 except $U_e = 20\,\mathrm{m\,s^{-1}}$.

seen in ZPG TBLs (see figure 10(a)). For $y^+ \leqslant 10$, the PTV data at all three flow speeds generally fall below the fit. The most likely cause of this consistent data-fit difference is an imperfect stretched-pixel-to-physical-coordinate conversion in the PTV image processing. An unintentional distortion of as little as a fraction of a wall unit could cause the deviations observed for $y^+ \leqslant 10$. A further indication of such unintentional distortion comes from the PTV-determined wall shear stress computed from $\mu(\mathrm{d}U/\mathrm{d}y)$ which is consistently several per cent below the force-balance-measured shear stress. Overall, for the inner flow fitting, noticeable data-fit differences can be explained by imperfection in the PTV image conversion from pixels to spatial coordinates.

As a final comparison, the current-TBL and the recommended ZPG-TBL fits from Monkewitz et al. (2007) are plotted in figure 10. The inner profile comparison, figure 10(a), shows clearly that the current fit lies above the ZPG fit for $y^+ > 5$ or so but is qualitatively similar. The outer profile comparison, figure 10(b), using the physical TBL parameters from $20\,\mathrm{m\,s^{-1}}$ and $x = 10.795\,\mathrm{m}$, shows the current fit above the ZPG fit for $y^+ < 25\,000$ or so. From there to the edge of the boundary layer, wake component differences cause the profiles to switch position and the current
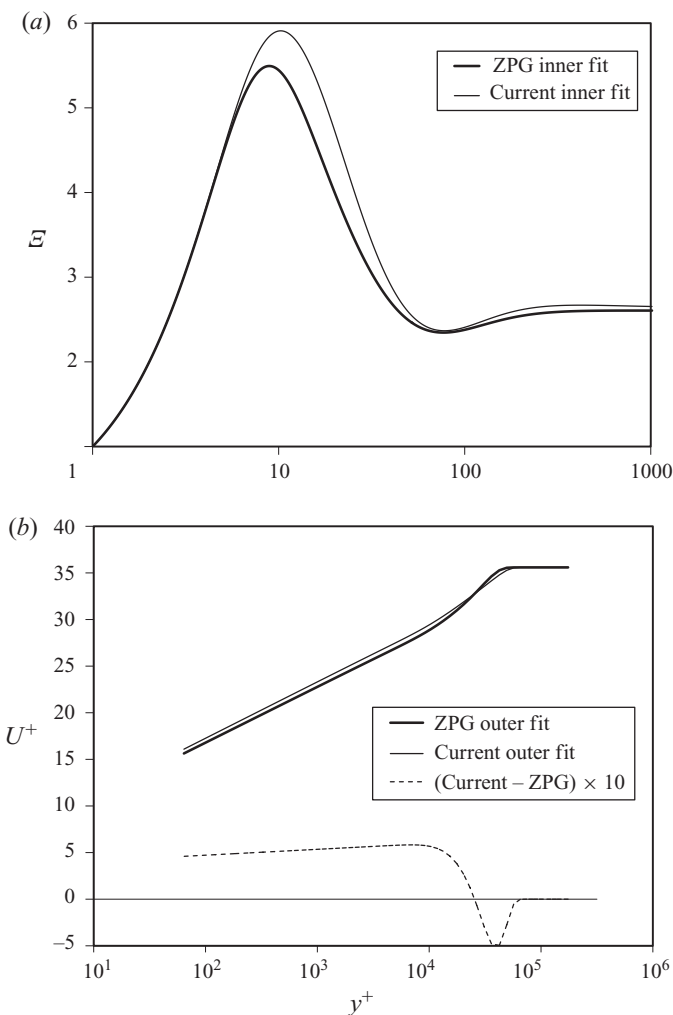
FIGURE 10. Comparison of the current and ZPG TBL profile fits. (*a*) Inner fit profile comparison in terms of the indicator function $\Xi = y^+(\mathrm{d}U^+_{inner}/\mathrm{d}y^+)$ versus y^+. The current inner profile falls above the ZPG profile, and both have extrema near $y^+ = 10$ and just below $y^+ = 100$. (*b*) Outer fit profile comparison in terms of U^+ versus y^+ at $U_e = 20\,\mathrm{m\,s^{-1}}$ and $x = 10.795\,\mathrm{m}$. The current outer profile is above the ZPG result for $y^+ < 25\,000$, but has a smaller wake component and falls below the ZPG result for $y^+ > 30\,000$ out to the edge of the boundary layer.

profile falls below the ZPG profile. A comparison of the fit-to-fit difference in figure 10(*b*) with the data-fit differences in figures 7–9 part (*a*) shows that the current profiles would not match the ZPG TBL profile recommended by Monkewitz *et al.* (2007) to within experimental error. Thus, a mild pressure gradient has a clear effect on high-Reynolds-number TBLs that extend from the near-wall region to the wake.

4. Summary and conclusions

This paper presents the results from an experimental investigation into the mean flow characteristics of the high-Reynolds-number TBL that formed on the largest possible flat-plate test model that could be fit into the world's largest low-turbulence

water tunnel. The reported streamwise velocity profiles are possibly unique in their completeness at the Reynolds numbers of these experiments, $Re_\theta \sim 10^5$ (or $Re_x \sim 10^8$). These results partially fill the gap between most laboratory-scale TBL investigations, and very high-Reynolds-number rough wall TBL studies and marine transportation applications. The results presented here include measurements of static pressure, skin friction and mean streamwise velocity at wall-normal distances from less than one wall unit to more than twice the TBL thickness. The experiments were well-controlled: the plate was hydrodynamically smooth, the water tunnel turbulence level was less than 0.4 % and the test conditions were repeatable to within instrumentation uncertainty. Velocity profile results at three Reynolds numbers – spanning a factor of three – are reported and fitted with inner and outer empirical forms.

One primary and two secondary conclusions are drawn from this study. First, the traditional TBL scaling and Reynolds-number dependence embodied in the ZPG TBL profile forms recommended in Monkewitz *et al.* (2007) are sufficient to fit the features of the current TBL mean velocity profiles for $54\,000 \leqslant Re_\theta \leqslant 156\,000$. One inner and one outer profile form was successfully fit to six measured mean streamwise velocity profiles to within experimental error, and these fitted profiles satisfy the von Kármán boundary-layer integral equation to within 1 %. Although the particular fitting constants determined in this investigation may unintentionally include experimental artefacts, the Reynolds-number dependence of the fitting drawn from classical TBL asymptotics is validated by this study.

Second, a mild pressure gradient appears to produce some obvious and subtle velocity profile differences when compared to an equivalent ZPG TBL profile. The obvious (and expected) difference is a smaller wake-flow component in the outer flow profile. The more subtle profile differences extend from slightly below to slightly above the buffer region, $5 < y^+ < 100$, and include mild modifications of the logarithmic-law constants. The current fit-determined values of κ and B from this study are lower and higher, respectively than ZPG TBL values. Interestingly, these deviations all work to place the current TBL profiles at or above an equivalent ZPG TBL profile from the wall to the wake region of the flow, and such deviations – faster flow at the same wall-normal location – are consistent with a mildly accelerating free stream.

And third, as a direct extension of the second conclusion, a mild pressure gradient produces a non-universal wall layer in high-Reynolds-number TBLs. This conclusion is consistent with a recent assessment of the log-law constants in wall-bounded flows (Nagib & Chauhan 2008) and a detailed study of favourable pressure gradient TBLs (Bourassa & Thomas 2009) that document the influence of pressure gradients on the log-law constants, and the extreme sensitivity of the Kármán constant to weak streamwise flow acceleration.

Appendix

PTV data

6.7 m s^{-1} y (mm)	x = 10.68 m U (m s^{-1})	13 m s^{-1} y (mm)	x = 10.68 m U (m/s)	20 m s^{-1} y (mm)	x = 10.68 m U (m s^{-1})
0.002351625	0.073877272	0.00156775	0.34020448	0.001371781	0.64178983
0.007054875	0.27050876	0.00470325	0.53155872	0.004115344	0.82547905
0.011758125	0.45270258	0.00783875	1.1636617	0.006858906	2.3110749
0.016461375	0.62410983	0.01097425	1.5480119	0.009602469	2.8544761
0.021164625	0.78787131	0.01410975	1.9578371	0.012346031	3.5919655
0.025867875	0.97246683	0.01724525	2.3597874	0.015089594	4.2612989
0.030571125	1.1481034	0.02038075	2.7215238	0.017833156	4.8638837
0.035274375	1.3071029	0.02351625	3.1163797	0.020576719	5.3950648
0.039977625	1.4629362	0.02665175	3.3689755	0.023320281	5.8403523
0.044680875	1.6069968	0.02978725	3.6273453	0.026063844	6.1572322
0.049384125	1.7342599	0.03292275	3.8644111	0.028807406	6.4964804
0.054087375	1.8390319	0.03605825	4.0660649	0.031550969	6.7326774
0.058790625	1.9478453	0.03919375	4.2602017	0.034294531	6.9576935
0.063493875	2.0384764	0.04232925	4.4160688	0.037038094	7.134165
0.068197125	2.1267365	0.04546475	4.5815266	0.039781656	7.3745647
0.072900375	2.205725	0.04860025	4.6844096	0.042525219	7.4769426
0.077603625	2.2740556	0.05173575	4.7976721	0.045268781	7.5824412
0.082306875	2.3352947	0.05487125	4.9163659	0.048012344	7.7304359
0.087010125	2.3825241	0.05800675	4.9953501	0.050755906	7.8497541
0.091713375	2.431725	0.06114225	5.0588998	0.053499469	7.9181912
0.096416625	2.4957088	0.06427775	5.1460858	0.056243031	8.0682121
0.10111987	2.542062	0.06741325	5.2044301	0.058986594	8.0780866
0.10582312	2.5710207	0.07054875	5.270063	0.061730156	8.1345998
0.11052638	2.6128182	0.07368425	5.3451172	0.064473719	8.2771843
0.11522963	2.6434548	0.07681975	5.3985806	0.067217281	8.3151159
0.11993287	2.6830675	0.07995525	5.4318815	0.069960844	8.3341598
0.12463613	2.7078064	0.08309075	5.5165699	0.072704406	8.4251694
0.12933937	2.738648	0.08622625	5.5336934	0.075447969	8.4730749
0.13404262	2.761792	0.08936175	5.5443165	0.078191531	8.5283171
0.13874587	2.7752861	0.09249725	5.5887506	0.080935094	8.5996484
0.14344912	2.8155805	0.09563275	5.6461234	0.083678656	8.6126007
0.14815237	2.8337862	0.09876825	5.6692353	0.086422219	8.7031344
0.15285563	2.8487954	0.10190375	5.6946883	0.089165781	8.7047761
0.15755888	2.8717626	0.10503925	5.7605564	0.091909344	8.7833008
0.16226213	2.883309	0.10817475	5.7836667	0.094652906	8.7780841
0.16696538	2.9059565	0.11131025	5.8162187	0.097396469	8.8484003
0.17166863	2.9228969	0.11444575	5.8381359	0.10014003	8.8516008
0.17637187	2.936297	0.11758125	5.8572779	0.10288359	8.9245268
0.18107512	2.9555239	0.12071675	5.8839632	0.10562716	8.9362953
0.18577837	2.9738865	0.12385225	5.9080717	0.10837072	8.9647576
0.19048162	2.9786245	0.12698775	5.9170634	0.11111428	9.0148785
0.19518487	2.9951142	0.13012325	5.9509261	0.112878	9.0257428
0.19988813	2.9998408	0.13325875	5.9629397	0.137962	9.3093394
0.20459138	3.0213055	0.13639425	5.9713975	0.163046	9.5248578
0.20929463	3.0326925	0.137962	6.001396	0.18813	9.7209815
0.21399788	3.0395625	0.163046	6.1601394	0.213214	9.884756
0.21870112	3.0608804	0.18813	6.2809599	0.238298	10.049308
0.22340437	3.0695415	0.213214	6.4017732	0.263382	10.175437
0.22810762	3.073047	0.238298	6.4960036	0.288466	10.323497
0.23281087	3.0854499	0.263382	6.6025863	0.31355	10.433378
0.23751412	3.0945421	0.288466	6.6755031	0.338634	10.554229
0.24221737	3.1067272	0.31355	6.7606452	0.363718	10.667456
0.24692062	3.1165684	0.338634	6.8311244	0.388802	10.757066

0.25162388	3.1253378	0.363718	6.8884774	0.413886	10.870123
0.25632712	3.1308337	0.388802	6.9543848	0.43897	10.937579
0.26103038	3.1508769	0.413886	7.0225043	0.464054	11.028552
0.263382	3.1488699	0.426428	7.0584187	0.489138	11.103916
0.288466	3.194914	0.451512	7.1047807	0.514222	11.188094
0.31355	3.2331498	0.476596	7.1719333	0.5487125	11.287194
0.338634	3.2684683	0.50168	7.2147456	0.5737965	11.350626
0.363718	3.3032295	0.526764	7.2691277	0.5988805	11.417315
0.388802	3.3356172	0.551848	7.3124926	0.6239645	11.478349
0.413886	3.3656881	0.576932	7.3617155	0.6490485	11.544281
0.43897	3.3941777	0.602016	7.4022159	0.6741325	11.59882
0.464054	3.4201848	0.6271	7.4410924	0.6992165	11.667666
0.489138	3.4461652	0.652184	7.4842892	0.7243005	11.71552
0.514222	3.4732923	0.677268	7.5230971	0.7493845	11.765545
0.539306	3.4988358	0.702352	7.5539606	0.7744685	11.806567
0.56439	3.51991	0.727436	7.5932346	0.7995525	11.882145
0.589474	3.5426764	0.75252	7.6307476	0.8246365	11.921719
0.614558	3.562815	0.777604	7.6592978	0.8497205	11.964486
0.639642	3.5841293	0.802688	7.6933548	0.8748045	12.007793
0.664726	3.6021884	0.827772	7.7283989	0.8998885	12.059527
0.68981	3.6249312	0.852856	7.7538384	0.9249725	12.100854
0.714894	3.6431947	0.87794	7.7807934	0.9500565	12.151162
0.739978	3.6606597	0.903024	7.8173518	0.9751405	12.183058
0.765062	3.6752065	0.928108	7.8439976	1.0002245	12.21905
0.790146	3.695642	0.953192	7.8710231	1.0253085	12.262688
0.81523	3.7110198	0.978276	7.9053877	1.0503925	12.29881
0.840314	3.7259438	1.00336	7.9274828	1.0754765	12.340124
0.865398	3.7416328	1.028444	7.9553258	1.1005605	12.362531
0.890482	3.7544316	1.053528	7.9751096	1.1256445	12.402433
0.915566	3.7670349	1.078612	8.0025938	1.1507285	12.454463
0.94065	3.7818273	1.103696	8.0229406	1.1758125	12.517744
		1.12878	8.0520436		
		1.153864	8.0862639		

LDV data
here, *ynot* is the local offset of the vertical coordinate *y*.

6.7 m s⁻¹ $y not =$ y (mm)	x = 10.555 m −0.06 mm U	x = 10.795 m 0.08 mm U	13 m s⁻¹ $y not =$ y (mm)	x = 10.555 m 0.34 mm U	x = 10.795 m 0.40 mm U	20 m s⁻¹ $y not =$ y (mm)	x = 10.555 m 0.02 mm U	x = 10.795 m 0.19 mm U
300	6.69771	6.72689	300		13.41799	300	20.17179	20.30939
260	6.67908	6.69802	260		13.41922	260	20.19345	20.17717
235	6.69304	6.69805	235	13.34706	13.36394	235	20.22052	20.18445
210	6.69215	6.69761	210	13.35300	13.36593	210	20.19510	20.19310
180	6.68172	6.70961	180	13.33108	13.38846	180	20.16631	20.23488
160	6.68511	6.71784	160	13.35379	13.41677	160	20.16639	20.27404
145	6.68142	6.71236	145	13.35413	13.41879	145	20.18439	20.25489
128	6.68951	6.70989	128	13.36397	13.41113	128	20.20401	20.22592
112	6.67485	6.69375	112	13.34786	13.37289	112	20.16363	20.19225
98	6.66747	6.65869	98	13.32918	13.31690	98	20.17219	20.06931
85	6.62149	6.61097	85	13.25549	13.24402	85	20.05886	19.98944
73	6.53545	6.50317	73	13.08813	13.02641	73	19.83712	19.76264
62	6.40551	6.38686	62	12.86332	12.83686	62	19.51169	19.37057
53.5	6.27070	6.27076	53.5	12.58164	12.59334	53.5	19.14210	19.10389
46	6.15074	6.13898	46	12.34486	12.34748	46	18.76860	18.72638
40	6.03702	6.03447	40	12.09102	12.13125	40	18.40955	18.39674
35	5.92911	5.91965	35	11.89858	11.93044	35	18.07869	18.08033
30.5	5.81033	5.81467	30.5	11.70343	11.69770	30.5	17.82662	17.76542
26.5	5.69582	5.74468	26.5	11.51665	11.52387	26.5	17.54254	17.50808

23	5.63438	5.64416	23	11.32384	11.33576	23	17.19313	17.22429
20.6	5.55396	5.56096	20.6	11.17436	11.19245	20.6	17.03444	17.00970
18	5.46755	5.49408	18	11.05895	11.08586	18	16.81616	16.77708
15.9	5.40002	5.42344	15.9	10.89562	10.87536	15.9	16.60248	16.54168
14.1	5.33727	5.33627	14.1	10.75826	10.71644	14.1	16.42172	16.35114
12.4	5.26562	5.24742	12.4	10.60423	10.60211	12.4	16.15583	16.10103
10.8	5.19484	5.21893	10.8	10.46645	10.41468	10.8	15.99973	15.96624
9.5	5.12173	5.10563	9.5	10.33743	10.32061	9.5	15.79328	15.70192
8.3	5.05296	5.03971	8.3	10.16025	10.17999	8.3	15.58654	15.50047
7.35	4.98345	4.97931	7.35	10.04217	10.06196	7.35	15.42271	15.33642
6.4	4.91733	4.91419	6.4	9.88126	9.89004	6.4	15.20428	15.12630
5.5	4.84206	4.80932	5.5	9.76438	9.78316	5.5	14.98420	14.90594
4.8	4.75785	4.73885	4.8	9.62126	9.59854	4.8	14.78151	14.73876
4.25	4.69299	4.70483	4.25	9.46135	9.44983	4.25	14.59146	14.50191
3.75	4.64793	4.60908	3.75	9.34988	9.32634	3.75	14.42645	14.35669
3.3	4.58039	4.55527	3.3	9.16885	9.18680	3.3	14.24504	14.14412
2.9	4.49597	4.48519	2.9	8.98384	9.01822	2.9	13.97169	13.91981
2.55	4.42847	4.38752	2.55	8.91452	8.86225	2.55	13.82998	13.70047
2.25	4.35580	4.32296	2.25	8.74962	8.71302	2.25	13.66460	13.48523
2	4.28309	4.26263	2	8.59167	8.57384	2	13.46181	13.32227
1.75	4.21199	4.15102	1.75	8.35440	8.34536	1.75	13.28095	13.05928
1.55	4.15101	4.08739	1.55	8.23259	8.21392	1.55	13.07493	12.83159
1.35	4.07765	4.03120	1.35	8.10588	7.99365	1.35	12.95717	12.60842
1.2	4.03115	3.95501	1.2	7.91679	7.84021	1.2	12.76188	12.39835
1.05	3.94965	3.88624	1.05	7.69501	7.60673	1.05	12.52206	12.15730
0.9	3.86784	3.78640	0.9	7.44205	7.29090	0.9	12.27603	11.82572
0.75	3.78278	3.70123	0.75	7.13035	6.98785	0.75	11.98554	11.49670
0.6	3.65233	3.53090	0.6	6.63760	6.44547	0.6	11.65202	11.10350
0.5	3.57756	3.41364	0.5	6.28708	5.72360	0.5	11.35187	10.60593
0.4	3.46816	3.31577	0.4			0.4	10.84317	10.16623
0.3	3.33202		0.3			0.3	10.42296	8.80553
0.2	3.17295		0.2			0.2	9.98619	
0.1			0.1			0.1		
0			0			0		

REFERENCES

AFZAL, N. 2001 Power law and log law velocity profiles in turbulent boundary layer flow: equivalent relations at large Reynolds numbers. *Acta Mechanica* **151**, 195–216.

BARENBLATT, G. I., CHORIN, A. J. & PROSTOKISHIN, V. M. 2000 A note on the intermediate region in turbulent boundary layers. *Phys. Fluids* **12**, 2159–2161.

BENEDICT, R. P. 1984 *Fundamentals of Pressure, Temperature and Flow Measurements*, pp. 340–349. Wiley.

BOURASSA, C. & THOMAS, F. O. 2009 An experimental investigation of a highly accelerated turbulent boundary layer. *J. Fluid Mech.* **634**, 359–404.

BUSCHMANN, M. H. & GAD-EL-HAK, M. 2003 Debate concerning the mean-velocity profile of a turbulent boundary layer. *AIAA J.* **41**, 565–572.

COMPTON D. A. & EATON J. K. 1996 A high resolution laser Doppler anemometer for three dimensional turbulent boundary layers. *Exp. Fluids* **22**, 111–117.

COMPTON D. A. & EATON J. K. 1997 Near-wall measurements in a three-dimensional turbulent boundary layer. *J. Fluid Mech.* **350**, 189–208.

DEGRAAFF, D. B. & EATON J. K. 2000 Reynolds-number scaling of the flat-plate turbulent boundary layer. *J. Fluid Mech.* **422**, 319–346.

ELBING, B. R., WINKEL, E. S., LAY, K. A., CECCIO, S. L., DOWLING, D. R. & PERLIN, M. 2008 Bubble-induced skin friction drag reduction and the abrupt transition to air-layer drag reduction. *J. Fluid Mech.* **612**, 201–236.

ETTER, R. J., CUTBIRTH, J. M., CECCIO, S. L., DOWLING, D. R. & PERLIN, M. 2005 High Reynolds number experimentation in the US Navy's William B. Morgan Large Cavitation Channel. *Meas. Sci. Technol.* **16**, 1701–1709.

FERNHOLTZ, H. H. & FINLEY, P. J. 1996 The incompressible zero-pressure-gradient turbulent boundary layer: an assessment of the data. *Prog. Aerosp. Sci.* **32**, 245–311.

FERNHOLTZ, H. H., KRAUSE, E., NOCKERMANN, M. & SCHOBER, M. 1995 Comparative measurements of the canonical boundary layer at $Re\delta_2 \leqslant 1.15 \times 10^5$ on the wall of the German–Dutch windtunnel. *Phys. Fluids* **7**, 1275–1281.

FIFE, P., WEI, T., KLEWICKI, J. & MCMURTRY, P. 2005 Stress gradient balance layers and scale hierarchies in wall-bounded turbulent flows. *J. Fluid Mech.* **532**, 165–189.

GAD-EL-HAK, M. & BANDYOPADHYAY, P. R. 1994 Reynolds number effects in wall-bounded turbulent flows. *Appl. Mech. Rev.* **47**, 307–365.

GEORGE, W. K. & CASTILLO, L. 1997 Zero-pressure-gradient turbulent boundary layer. *Appl. Mech. Rev.* **50**, 689–729.

KNOBLOCK, K. & FERNHOLTZ, H.-H. 2002 Statistics, correlations, and scaling in a turbulent boundary layer at $Re\iota_2 \leqslant 1.15 \times 10^5$. In *IUTAM Symposium on Reynolds Number Scaling in Trubulent Flow* (ed. A. J. Smits), pp. 11–16. Springer.

KUNKEL, G. J. & MARUSIC, I. 2006 Study of the new-wall-turbulent region of the high Reynolds number boundary layer using an atmospheric flow. *J. Fluid Mech.* **548**, 375–402.

LAUNDER, B. E. & SPALDING, D. B. 1972 *Mathematical Models of Turbulence*. Academic Press.

LINDGREN, B., ÖSTERLUND, J. M. & JOHANSSON, A. V. 2004 Evaluation of scaling laws derived from Lie group symmetry methods in zero-pressure-gradient turbulent boundary layers. *J. Fluid Mech.* **502**, 127–152.

MARUSIC, I. & KUNKEL, G. J. 2003 Streamwise turbulence intensity formulation for flat-plate boundary layers. *Phys. Fluids* **15**, 2461–2464.

MARUSIC, I., MCKEON, B. J., MONKEWITZ, P. A., NAGIB, H. M., SMITS, A. J. & SREENIVASAN, K. R. 2010 Wall bounded turbulent flows at high Reynolds numbers: recent advances and key issues. *Phys. Fluids* **22**, 065103.

MARUSIC, I., UDDIN, A. K. M. & PERRY, A. E. 1997 Similarity law for the streamwise turbulence intensity in zero-pressure-gradient turbulent boundary layers. *Phys. Fluids* **9**, 3718–3726.

MCKEON, B. (ed.) 2007 Theme issue on scaling and structure in high Reynolds number wall bounded flows. *Phil. Trans. R. Soc. Lond.*, Ser. A **365**, 635–876.

METZGER, M. M. & KLEWICKI, J. C. 2001 A comparative study of near-wall turbulence in high and low Reynolds number boundary layers. *Phys. Fluids* **13**, 692–701.

METZGER, M. M., KLEWICKI, J. C., BRADSHAW, K. L. & SADR, R. 2001 Scaling the near-wall axial turbulent stress in the zero pressure gradient boundary layer. *Phys. Fluids* **13**, 1819–1821.

MONKEWITZ, P. A., CHAUHAN, K. A. & NAGIB, H. M. 2007 Self-consistent high-Reynolds number asymptotics for zero-pressure-gradient turbulent boundary layers. *Phys. Fluids* **19**, 115101.

MONKEWITZ, P. A., CHAUHAN, K. A. & NAGIB, H. M. 2008 Comparison of mean flow similiarity laws in zero pressure gradient turbulent boundary layers. *Phys. Fluids* **20**, 105102.

NAGIB, H. M. & CHAUHAN, K. A. 2008 Variations of the von Kármán coefficient in canonical flows. *Phys. Fluids* **20**, 101518.

NAGIB, H. M., CHRISTOPHOROU, C. & MONKEWITZ, P. A. 2004 High Reynolds number turbulent boundary layers subjected to various pressure-gradient conditions. In *IUTAM Symposium on One Hundred Years of Boundary Layer Research* (ed. G. Meier & K. Sreenivasan), pp. 383–394. Springer.

ÖSTERLUND, J. M., JOHANSSON, A. V., HAGIB, H. M. & HITES, M. H. 1999 Wall shear stress measurements in high Reynolds number boundary layers from two facilities. In *30th AIAA Fluid Dynamics Conference*, Norfolk, VA (AIAA Paper no. 99–3814).

ÖSTERLUND, J. M., JOHANSSON, A. V. & NAGIB, H. 2000a A note on the overlap region in turbulent boundary layers. *Phys. Fluids* **12**, 1–4.

ÖSTERLUND, J. M., JOHANSSON, A. V., NAGIB, H. & HITES, M. H. 2000b Comment on 'A note on the intermediate region in turbulent boundary layers [*Phys. Fluids* 12, 2159]'. *Phys. Fluids* **12**, 2360–2363.

PANTON, R. C. 2002 Evaluation of the Barenblatt–Chorin–Prostokishin power law for turbulent boundary layers. *Phys. Fluids* **14**, 180-1808.

PARK, J. T., CUTBIRTH, J. M. & BREWER, W. H. 2003 Hydrodynamic performance of the Large Cavitation Channel (LCC). In *Proceedings of the 4th ASME_JSME Joint Fluids Engng Conference*, Honolulu, HI.

POPE, S. B. 2000 *Turbulent Flows*. Cambridge University Press.

SADDOUGHI, S. G. & VEERAVALLI, S. V. 1994 Local isotropy in turbulent boundary layers at high Reynolds numbers. *J. Fluid Mech.* **268**, 333–372.

SANDERS, W. C., WINKEL, E. S., DOWLING, D. R., PERLIN, M. & CECCIO, S. L. 2006 Bubble friction drag reduction in a high Reynolds number flat plate turbulent boundary layer. *J. Fluid Mech.* **552**, 353–380.

SCHULTZ-GRUNOW, F. 1941 New frictional resistance law for smooth plates. *NACA Tech. Memorandum* 17–18, 1–24.

SREENIVASAN, K. R. 1989 The turbulent boundary layer. *Frontiers Exp. Fluid Mech.* **46**, 159–209.

WEI, T., FIFE, P., KLEWICKI, J. & MCMURTRY, P. 2005 Properties of the mean momentum balance in turbulent boundary layer, pipe, and channel flows. *J. Fluid Mech.* **522**, 303–327.

WHITE, F. M. 2006 *Viscous Fluid Flow*, 3rd edn. McGraw-Hill.

WINKEL, E. S., OWEIS, G. F., VANAPALLI, S. A., DOWLING, D. R., PERLIN, M., SOLOMOM, M. J. & CECCIO, S. L. 2009 High Reynolds number turbulent boundary layer friction drag reduction from wall-injected polymer solutions. *J. Fluid Mech.* **621**, 259–288.